Structural Changes in the Cytoplasmic Domain of Phospholamban by Phosphorylation at Ser16: A Molecular Dynamics Study†

Yuji Sugita,‡,§ Naoyuki Miyashita,‡,|| Takao Yoda,⊥ Mitsunori Ikeguchi,@ and Chikashi Toyoshima*,‡

Institute of Molecular and Cellular Biosciences, The University of Tokyo, 1-1-1 Yayoi, Bunkyo-ku, Tokyo 113-0032, Japan, CREST, Japan Science and Technology Agency, 4-1-8 Honcho Kawaguchi, Saitama, Japan, Nagahama Institute of Bio-Science and Technology, Tamura, Nagahama, Shiga 526-0829, Japan, and Graduate School of Integrated Science, Yokohama City University, Suehirocho 1-7-29, Tsurumi-ku, Yokohama 230-0045, Japan

Received May 30, 2006; Revised Manuscript Received August 8, 2006

ABSTRACT: Phospholamban is a 52-residue integral membrane protein that regulates the activity of the sarcoplasmic reticulum calcium pump in cardiac muscle. Its inhibitory action is relieved when phospholamban is phosphorylated at Ser16 by cAMP-dependent protein kinase. To computationally explore all possible conformations of the phosphorylated form, and thereby to understand the structural effects of phosphorylation, replica-exchange molecular dynamics (REMD) was applied to the cytoplasmic domain that includes Ser16. The simulations showed that (i) without phosphorylation, the region from Lys3 to Ser16 takes all α-helical conformations; (ii) when phosphorylated, the α-helix is partially unwound in the C-terminal part (from Ser10 to Ala15) resulting in less extended conformations; (iii) the phosphate at Ser16 forms salt bridges with Arg9, Arg13, and/or Arg14; and (iv) the salt bridges with Arg13 and Arg14 distort the α-helix and induce unwinding of the C-terminal part. We then applied conventional all-atom molecular dynamics simulations to the full-length phospholamban in the phospholipid bilayer. The results were consistent with those obtained with REMD simulations, suggesting that the transmembrane part of phospholamban and the lipid bilayer itself have only minor effects on the conformational changes in the cytoplasmic domain. The distortions caused by the salt bridges involving the phosphate at Ser16 readily explain the relief of the inhibitory effect of phospholamban by phosphorylation, as they will substantially reduce the population of all helical conformations, which are presumably required for the binding to the calcium pump. This will also be the mechanism for releasing the phosphorylated phospholamban from kinase.

Phospholamban (PLN)[1] is an integral membrane protein of 52 amino acid residues and works as a reversible inhibitor of the sarcoplasmic reticulum Ca^{2+}-ATPase (SERCA) in cardiac muscle (*1*). According to recent NMR structure determinations (*2*), the cytoplasmic part (residues 1−21) comprises an α-helix (domain Ia, residues 1−16) connected to the transmembrane helix (domain II, residues 22−52) by a flexible linker (domain Ib). Binding of PLN to SERCA reduces the rate of uptake of Ca^{2+} into the reticulum, whereas phosphorylation of PLN at Ser16 by cAMP-dependent protein kinase (PKA) (*3*) or at Thr17 by Ca^{2+}/calmodulin-dependent kinase relieves the inhibition (*4*). Although several NMR structure studies have been published for unphosphorylated PLN alone (*2*, *5*), no atomic structure is available for phosphorylated PLN (pPLN) or those bound to SERCA, yet extensive mutagenesis (*6*, *7*) and cross-linking studies (*8*) led us to propose an atomic model of unphosphorylated PLN bound to SERCA (*9*), based on the crystal structure of skeletal muscle Ca^{2+}-ATPase (SERCA1a) in the absence of Ca^{2+} (*10*). In the model, the PLN transmembrane helix fits into a groove formed by the M2, M4, M6, and M9 helices of SERCA1a, and the C-terminal part of the cytoplasmic helix of PLN is unwound so that Lys3 of PLN can be cross-linked with Lys397 and Lys400 in SERCA1a.

Structural information about PLN in membrane and in the PLN−SERCA complex has been gained by nuclear magnetic resonance (NMR) (*2*, *5*, *11*−*13*), electron paramagnetic resonance (*14*, *15*), and fluorescence resonance electron transfer (FRET) (*16*, *17*). However, the NMR and FRET studies did not provide a consistent picture of the structural changes in PLN caused by phosphorylation at Ser16. NMR studies of a mutant of PLN (AFA-PLN) that does not form oligomers (*18*, *19*) showed that the phosphorylation unwinds the C-terminal part of the cytoplasmic α-helix and shifts the conformational equilibrium toward a disordered state (*13*). They also suggested that a stable salt bridge involving the

† This work was supported in part by a Creative Science Project Grant (to C.T.) and a Grant for Scientific Research on a Priority Areas 'Membrane Interface' (to Y.S.) from the Ministry of Education, Culture, Sports, Science and Technology of Japan.

* To whom correspondence should be addressed: Institute of Molecular and Cellular Biosciences, The University of Tokyo, 1-1-1 Yayoi, Bunkyo-ku, Tokyo 113-0032, Japan. Telephone: +81-3-5841-8492. Fax: +81-3-5841-8492. E-mail: ct@iam.u-tokyo.ac.jp.

‡ The University of Tokyo.

§ Japan Science and Technology Agency.

|| Present address: Department of Chemistry, Boston University, Boston, MA 02215.

⊥ Nagahama Institute of Bio-Science and Technology.

@ Yokohama City University.

[1] Abbreviations: PLN, phospholamban; SERCA, sarco(endo)plasmic reticulum calcium ATPase; REMD, replica-exchange molecular dynamics method; PCA, principal component analysis; EPR, electron paramagnetic resonance; NMR, nuclear magnetic resonance; FRET, fluorescence resonance energy transfer.

10.1021/bi061071z CCC: $33.50
Published on Web 09/09/2006

phosphate at Ser16 is unlikely. In contrast, FRET studies suggested that pPLN takes more compact helical conformations stabilized by a salt bridge between Arg13 and the phosphate at Ser16 (*16*). The primary aim of this paper is to provide a unified picture of the structural changes in PLN caused by phosphorylation at Ser16 via all-atom molecular dynamics (MD) simulations of PLN and pPLN.

Similar efforts have been made by two groups so far, but only in 10−20 ns range (*20*, *21*). MD simulations of this time range are unlikely to be able to explore all relevant conformations of pPLN at room temperature. In particular, given the lack of experimentally determined atomic structure of pPLN that can be used as the starting structure, it is difficult to provide thermally equilibrated conformations of pPLN by conventional MD simulations on the nanosecond time scale. Therefore, we used replica-exchange molecular dynamics (REMD) (*22*) to explore all possible conformations of the cytoplasmic domain (residues 1−20) of PLN (PLN_C) and pPLN ($pPLN_C$) in solution. Like the other generalized-ensemble algorithms (*23*−*29*), this method enables sampling of a sufficiently wide conformational space of a target protein and likely provides a distribution of all relevant conformations at thermal equilibrium without an atomic structure experimentally determined. We then carried out conventional MD simulations of full-length PLN and pPLN in a lipid bilayer and studied the effects of the trasnsmembrane domain and the lipid bilayer itself. These simulations show that salt bridge formation involving Arg9 and the phosphate at Ser16 is likely to be the key event that results in the relief of inhibitory action of PLN.

MATERIALS AND METHODS

REMD. Here, we briefly describe how REMD (*22*) enhances conformational sampling of proteins or systems with rugged energy landscapes. In REMD simulations, a number of noninteracting copies of the original system (or replicas) at different temperatures are simulated independently and simultaneously by conventional MD. Every few steps, pairs of replicas are exchanged with a transition probability according to the Metropolis criteria (*25*). This exchange process generates a random walk of replicas in temperature space, which, in turn, induces a random walk in potential energy space. Because the random walk avoids trapping at one of the local energy minima, REMD simulations enable sampling of a wider conformational space than conventional MD simulations and ensure statistically reliable thermal averages at each temperature by using single-histogram (*30*) or multiple-histogram techniques (*31*, *32*).

Computational Details from the REMD Simulations of the Cytoplasmic Domain of PLN in Solution. REMD simulations of the cytoplasmic domain (residues 1−20) of PLN (PLN_C) or pPLN ($pPLN_C$) were performed with explicit solvents using a modified version of PRESTO (*33*−*35*). The C-termini of the proteins were blocked with an *N*-methyl group. The starting structure of PLN_C was taken from the corresponding region of the first conformer of the NMR structures reported by Zamoon et al. (PDB entry 1N7L) (*2*); for $pPLN_C$, it was prepared by simply changing the side chain of Ser16 to the phosphorylated form. PLN_C and $pPLN_C$ were solvated in a sphere with a radius of 30 Å, in which 8 K^+ ions, 11 Cl^- ions, and 3405 water molecules and 9 K^+ ions, 10 Cl^- ions, and 3399 water molecules were included, respectively (Figure 1a). The salt concentration in each system was set to 150 mM. Harmonic restraints were applied to prevent solvent molecules from exiting the sphere. CHARMM27

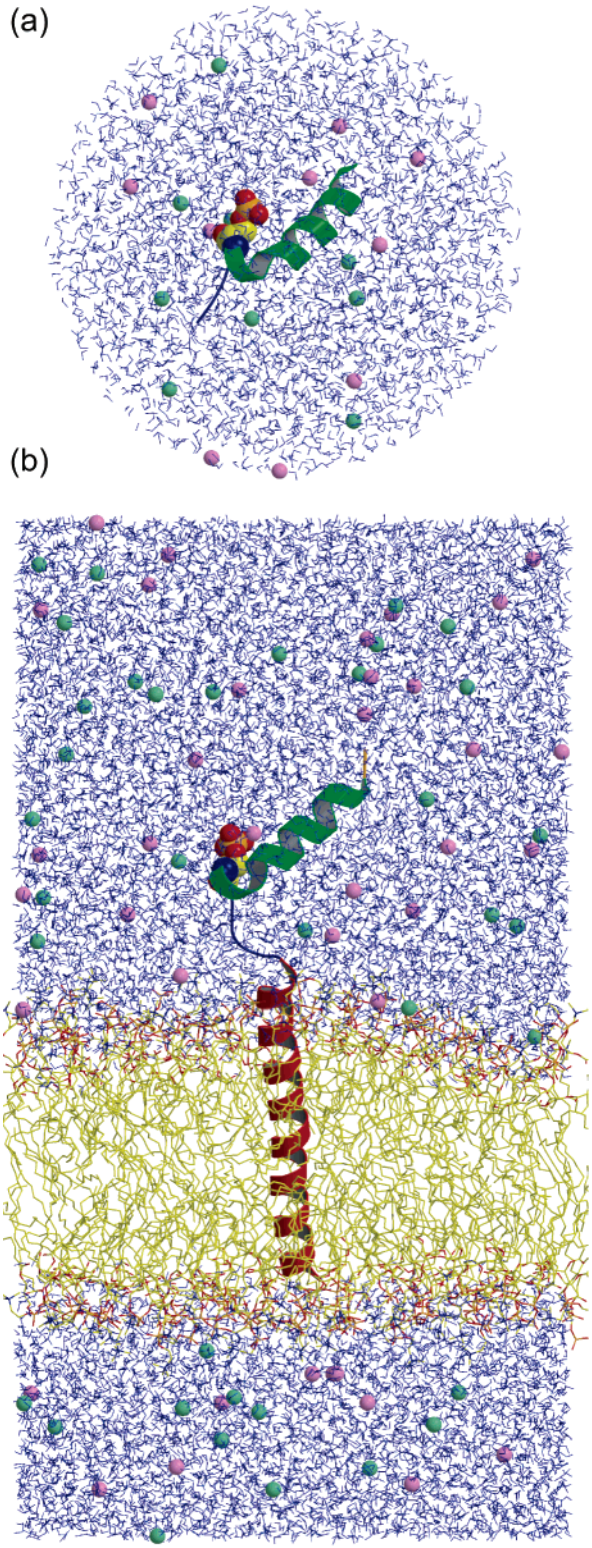

FIGURE 1: Starting structures of pPLN. (a) In the REMD simulation, the cytoplasmic domain (residues 1−20) of pPLN was solvated in 150 mM KCl. (b) In the MD simulations, full-length pPLN (residues 1−52) was simulated with 123 dioleoylphosphatidylcholine (DOPC) molecules and solvated in 150 mM KCl. This figure was prepared using Molscript (*58*) and Raster3D (*59*).

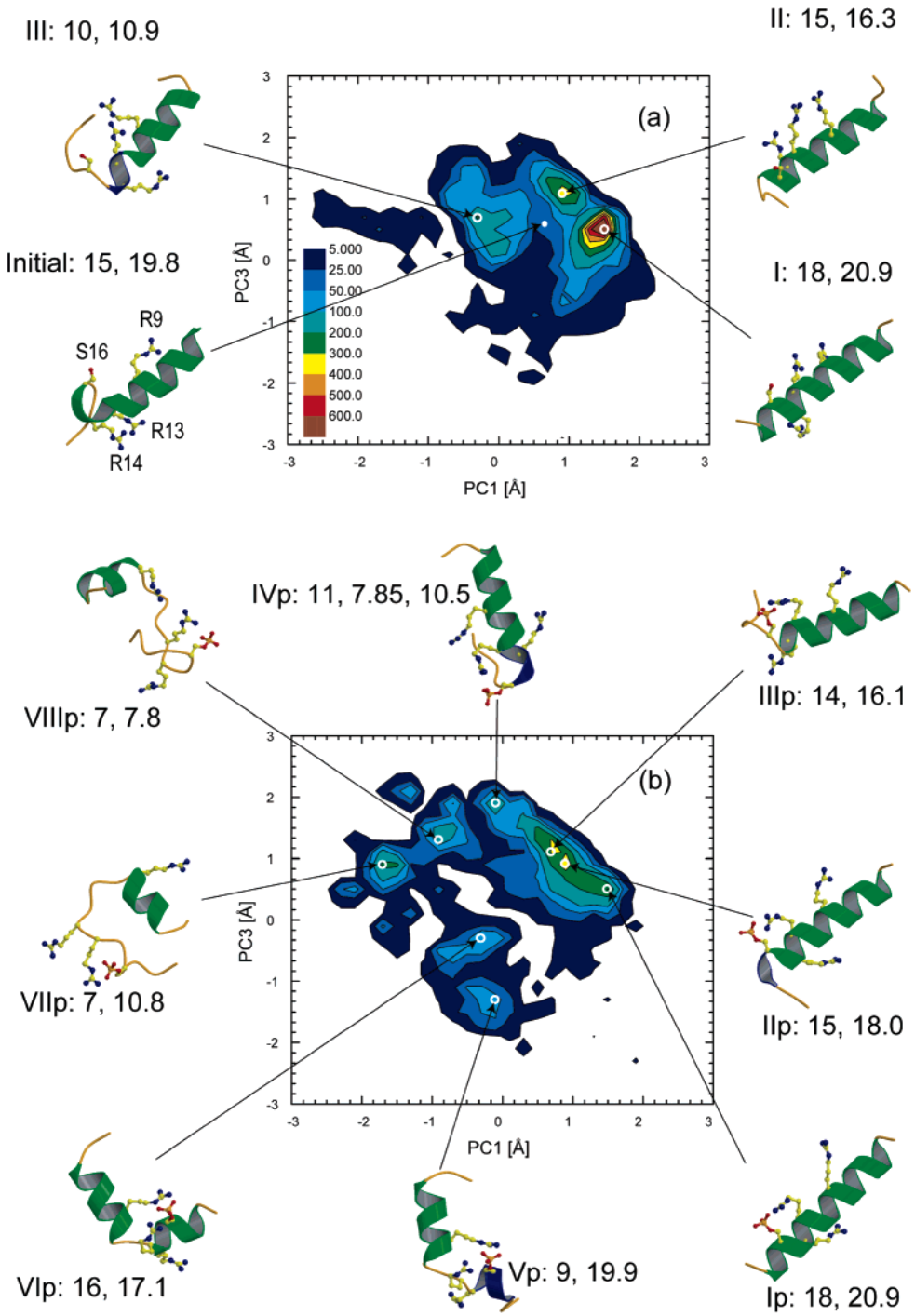

FIGURE 2: Free energy landscape of (a) PLN_C and (b) $pPLN_C$ at 310 K in the REMD calculations. The starting conformation of PLN_C (white circle) and the representative stable conformations at local energy minima (open circles) are also shown. The values are the number of α-helical residues and the Cα distance between Tyr6 and Met20 of the representative structure in each cluster. The side chains of Arg9, Arg13, Arg14, and Ser16 are represented in ball-and-stick form.

CMAP potential functions (*36*, *37*) were used for proteins, and the TIP3P model (*38*) was used for water molecules. The electrostatic interactions were computed using the cell multipole method (*39*). All bonds involving hydrogen atoms in proteins were constrained by LINCS (*40*), and water molecules were treated as rigid bodies by using SETTLE (*41*). The equation of motion was integrated with a time step of 1 fs by using a leapfrog algorithm.

Sixty replicas with different temperatures (290−653 K) were simulated for 8 and 10 ns in the simulations of PLN_C and $pPLN_C$, respectively. The total simulation lengths were 480 ns for PLN_C and 600 ns for $pPLN_C$. Replica exchanges were attempted every 100 steps. The quality of random walks in potential energy space was evaluated by counting the number of tunneling events in the respective simulations. Here, a tunneling event is defined as a trajectory from a sufficiently high energy (E_H) to a low energy (E_L) or from an E_L to an E_H. E_H and E_L were set to average energies at 603 and 310 K, respectively. The coordinates saved every 500 steps for the final 6 ns of the simulations were used for conformational analysis. To monitor the sampling efficiency in conformational space, we performed a principal compo-

nent (PC) analysis (*42*−*44*) on the simulation trajectories. The variance−covariance matrix was calculated using all heavy atom coordinates in each simulation and was diagonalized to obtain PC axes. To make the number of degrees of freedom in PC analysis identical for PLN_C and $pPLN_C$, we ignored the coordinates of the three oxygen atoms in phosphorylated Ser16 (pSer16) of $pPLN_C$.

Computational Details of the MD Simulations of Full-Length PLN in a Dioleoylphosphatidylcholine (DOPC) Membrane. Full-length PLN and pPLN were simulated with explicit solvent and phospholipids (DOPC) by using MARBLE (*45*). CHARMM27 CMAP parameters were used for proteins (*36*, *37*) and phospholipids (*46*), and the TIP3P model (*38*) was used for water. The full simulation system (PLN or pPLN, 123 DOPC molecules, and a 150 mM KCl salt solution) contained approximately 60 000 atoms, including more than 14 000 water molecules. The initial structure of PLN was taken from the 18th NMR structure (PDB entry 1N7L) (*2*), because it is the closest to the atomic model of PLN bound to SERCA (*9*). As shown in Figure 1b, when PLN was inserted into a DOPC membrane, its transmembrane helix was oriented in the same way as the atomic model. Periodic boundary conditions were used in the MD simulations, and the electrostatic interactions were computed without truncation using the particle mesh Ewald algorithm (*47*). All water molecules and all CH_x, NH_x ($x = 1$, 2, or 3), SH, and OH groups in protein and phospholipids were treated as rigid bodies (*45*). The equation of motion was integrated with a time step of 2 fs. The coordinates were saved every 500 steps. The pressure and temperature were set at 1 atm and 310 K, respectively, by using the constant area−isothermal isobaric algorithm (*45*, *48*, *49*). Before the production dynamics, a 600 ps equilibration was performed as described previously for MD simulations of the skeletal muscle sarcoplasmic reticulum Ca^{2+}-ATPase (*50*).

RESULTS

Performance of REMD Simulations. In this study, we used 60 replicas that were distributed between 290 and 653 K. Replica exchanges were attempted every 100 steps only for neighboring replicas and were accepted for 16−32% using the Metropolis criteria (*25*). In total, 95 and 137 tunneling events took place in the simulations of PLN_C and $pPLN_C$, respectively, indicating that the replica-exchange method worked properly.

Principal Component Analysis of PLN_C and $pPLN_C$. We first studied free energy landscapes of PLN_C and $pPLN_C$ by analyzing PCs of the simulation trajectories. The first (PC1) and third PC (PC3) axes were used to draw the landscapes at 310 K, as different local minima appeared more clearly in the PC1−PC3 plane than in the PC1−PC2 plane. Contributions to the mean square fluctuation from the second (PC2) and PC3 were similar (8.6 and 8.4%, respectively). Three major clusters were found in the free energy landscape of PLN_C (Figure 2a). In cluster I, PLN_C consisted of a long α-helix from Glu2 to Glu19, whereas the C-terminal part of the α-helix was unwound in clusters II (between Thr17 and Glu19) and III (between Ile12 and Glu19), suggesting that the structural ensemble of PLN in solution contains the conformations similar to that of the atomic model of PLN bound to SERCA (*9*). Interestingly, the NMR structure of the cytoplasmic domain of PLN (*2*), which was used as the starting model, was located almost at the midpoint among the three clusters.

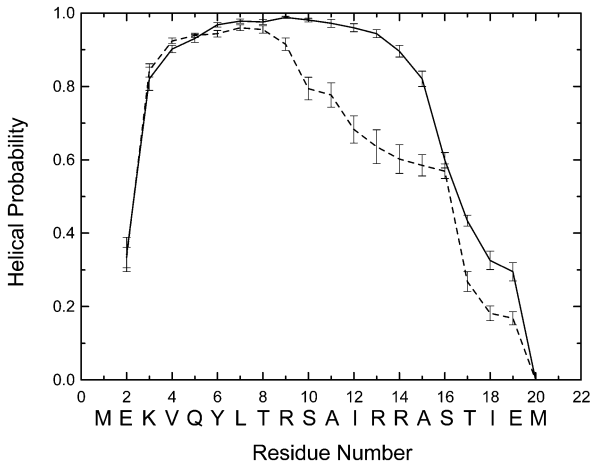

FIGURE 3: Average α-helicity of each residue in PLN (—) and pPLN (- - -) at 310 K. An α-helical residue was defined by the same criteria that were used in DSSP (*51*). The error bars show the standard error of block averages that were calculated for every 1 ns.

In contrast, the simulation of $pPLN_C$ exhibited a broader distribution in the free energy landscape comprising eight clusters, which were further classified into three groups (Figure 2b). In the first group (clusters Ip, IIp, IIIp, and IVp), $pPLN_C$ consisted of a long α-helix from Lys3 to pSer16 and contained, at most, a single salt bridge between pSer16 and Arg13. In the second group (Vp and VIp), two salt bridges were formed between the phosphate and two arginines (Arg9 and Arg13). Due to the two salt bridges, the C-terminal part of the α-helix was partially unwound or divided into two short helices. The third group (VIIp and VIIIp) contained disordered conformations, in which a salt bridge was formed between the phosphate and Arg14. Thus, phosphorylation of PLN at Ser16 formed salt bridges with arginines and increased the number of conformational substates by distorting the α-helix.

Backbone Structures of PLN_C and $pPLN_C$. To examine the structural changes between PLN_C and $pPLN_C$ more quantitatively, we calculated the α-helicity of each residue at 310 K with the same criteria as DSSP (*51*). In both PLN_C and $pPLN_C$, the first two (Met1 and Glu2) and last four (Thr17 and Met20) residues had low helicity whereas the region from Gln5 to Arg9 took an α-helical conformation with high probability (Figure 3). A marked difference was found with the region from Ser10 to Ala15: the α-helix in this region of PLN_C remained stable but unwound in $pPLN_C$.

We next analyzed the Cα distance between Tyr6 and Met20 to compare the simulation results with the FRET measurements (*16*, *17*). Figure 4 shows that the distribution for PLN_C has a sharp peak around 21.5 Å, whereas that for $pPLN_C$ has a broader distribution with a peak as short as 10.5 Å. At 310 K, the average distance in $pPLN_C$ (16.1 ± 0.8 Å) was ∼2 Å shorter than that in PLN_C (18.1 ± 0.8 Å). As shown in Figure 2, the structure with the sharp peak around 21.5 Å corresponds to an extended α-helix (clusters I, Ip, and IIp), whereas partially disordered ones (III, IVp, VIp, VIIp, and VIIIp) have shorter distances (8−17 Å).

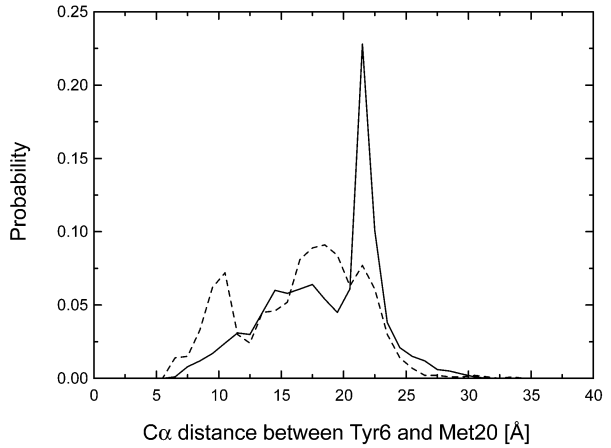

FIGURE 4: Distribution of the Cα distance between Tyr6 and Met20 at 310 K calculated with Cα atoms of PLN_C (—) and $pPLN_C$ (- - -) in the REMD simulations.

Table 1: Salt Bridges Observed in REMD Simulations of PLN and pPLN at 310 K

negatively charged residue involved in the salt bridge	positively charged residue involved in the salt bridge	probability of the formation of the salt bridge (%)	
		PLN	pPLN
Glu2	Lys3	2.1	2.4
Glu2	Arg9	3.8	3.5
Glu2	Arg9	2.9	0.0
Glu2	Arg14	0.0	1.4
pSer16[a]	Lys3	–	6.9
pSer16[a]	Arg9	–	28.2
pSer16[a]	Arg13	–	63.4
pSer16[a]	Arg14	–	21.5
Glu19	Lys3	0.5	3.1
Glu19	Arg9	9.3	13.5
Glu19	Arg13	16.3	13.8
Glu19	Arg14	11.6	25.1

[a] Phosphorylated Ser16.

Side Chain Interactions in the Cytoplasmic Domain of PLN. As described earlier, unwinding of the α-helix was correlated with salt bridge formation involving the phosphate at Ser16. We therefore more quantitatively examined how often such salt bridges are formed. Here, we define that a salt bridge is formed when the distance between an amide nitrogen atom and a carboxyl or phosphorus oxygen atom is ≤3.0 Å. Table 1 lists the probability of each salt bridge formation in the REMD simulations. PLN_C had only two salt bridges between Arg13 and Glu19 and between Arg14 and Glu19. These salt bridges are likely to act as terminators of the cytoplasmic α-helix. In addition to these, in $pPLN_C$ the phosphate at Ser16 formed salt bridges with Arg9, Arg13, and/or Arg14. Of these, the salt bridge between Arg13 and the phosphate was the one most frequently observed.

We next examined how salt bridges between the phosphate at Ser16 and the three arginines are related to the conformational disorders observed in $pPLN_C$. Table 2 lists the relationship between the frequency of salt bridges involving the phosphate and the average number of α-helical residues in $pPLN_C$. We identified four major groups for the salt bridge formations in $pPLN_C$: (i) a single salt bridge with Arg13 (38.1%), (ii) dual salt bridges with Arg9 and Arg13 (23.3%), (iii) a single salt bridge with Arg14 (12.9%), and (iv) no salt bridges (13.3%). A $pPLN_C$ in groups (i) and (iv) has more than 14 α-helical residues similar to PLN_C. In contrast, a $pPLN_C$ in groups (ii) and (iii) has fewer than 12 α-helical residues, indicating that the salt bridges involving Arg9 and Arg14 act as helix breakers in $pPLN_C$. The temperature dependence of salt bridge formation between the phosphate at Ser16 and Arg13 correlated with that of α-helix formation, whereas those with Arg9 and Arg14 correlated with that of the Cα distance between Tyr6 and Met20 (Figure 5), confirming the different roles of the salt bridges.

MD Simulations of Full-Length PLN and pPLN in Membranes. We next performed MD simulations of full-length PLN and pPLN with explicit solvent and a DOPC lipid bilayer to examine how lipid molecules affect the results obtained in the REMD simulations. For this purpose, we carried out MD simulations of full-length PLN and pPLN for 30 ns each, starting from the NMR structure. In another simulation of pPLN, to reflect the structures in the second group of $pPLN_C$ (clusters Vp and VIp in Figure 2b), we restrained the distance for the first 10 ns between the phosphorus oxygen atoms in pSer16 and the amide nitrogen atoms in Arg9 and Arg13. After the distance restraint was removed, the simulation was continued for an additional 20 ns. Hereafter, we refer to this simulation of pPLN as pPLN_rest.

In the simulations of PLN and pPLN, the cytoplasmic and transmembrane helices remained stable (Figure 6a,b and Figure 1 of the Supporting Information). In pPLN, the salt bridge between pSer16 and Arg13 formed spontaneously at ∼7 ns and remained stable until the end of the simulation. After the distance restraints in pPLN_rest were removed, the dual salt bridges between the phosphate at Ser16 and Arg9 and Arg13 remained intact (Figure 6c). Due to the salt bridges, the C-terminal part of the cytoplasmic α-helix was partially unwound and divided into two short helices. Other

Table 2: Classification of pPLN with the Number of Salt Bridges Involving the Phosphate at Ser16 Observed in the REMD Simulation of pPLN at 310 K

no. of salt bridges	residues that form salt bridges with pSer16[a]	probability of the formation of salt bridges (%)	average no. of α-helical residues	corresponding clusters in Figure 2b
0	–	13.3	14.1	IIp, IIIp
1	K3	0.2	6.3	–
1	R9	2.7	13.0	–
1	R13	38.1	14.2	Ip, IIp, IIIp, IVp
1	R14	12.9	9.7	VIIp, VIIIp
2	K3, R14	6.0	6.7	VIIp, VIIIp
2	R9, R13	23.3	11.5	Vp, VIp
2	R9, R14	1.4	0.5	–
2	R13, R14	1.2	5.3	–
3	K3, R9, R13	0.7	0	–

[a] The salt bridge patterns with occurrences of <0.1% are not listed here.

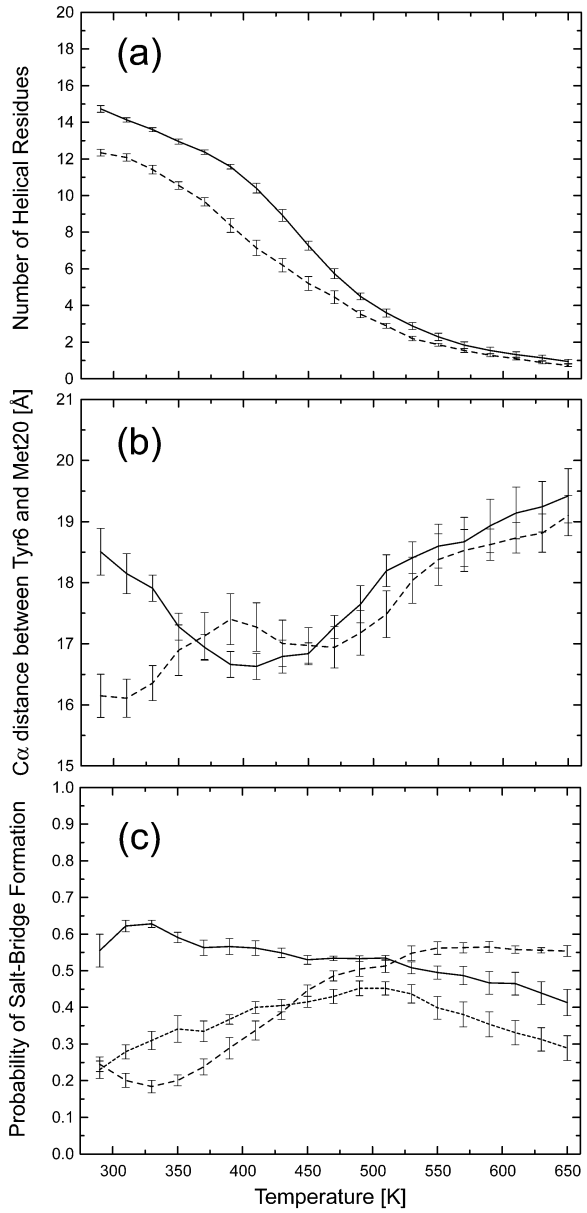

FIGURE 5: Temperature dependence of (a) the number of α-helical residues, (b) the Cα distance between Tyr6 and Met20, and (c) salt bridge formation. In panels a and b, solid and dashed lines represent the averaged values obtained in the REMD simulations of PLN_C and $pPLN_C$, respectively. In panel c, the probabilities of salt bridge formation between the phosphate at Ser16 and Arg9 (···), Arg13 (—), and Arg14 (- - -) obtained in the REMD simulation of $pPLN_C$ are shown. The error bars show the standard error of block averages that were calculated for every 1 ns.

structural parameters (e.g., α-helicity of each residue, R_g of the cytoplasmic domain, and the Cα distance between Tyr6 and Met20) observed in the MD simulations of PLN and pPLN in membranes were similar to those in the REMD simulations, although the distributions in the MD simulations were much narrower than those in the REMD simulations. This is as expected because the structures in conventional MD simulations are likely trapped at local energy minima near the starting conformations. The structural changes in the cytoplasmic domain appear to be hardly affected by the events in the transmembrane domain and lipid bilayer.

In simulations of full-length PLN and pPLN in a lipid bilayer, the angle between the cytoplasmic and transmembrane helices fluctuated rapidly between open and closed (L-shaped) conformations (Figure 7a). Starting from an open conformation of PLN, which is the closest to the atomic model of PLN bound to SERCA, we observed the L-shaped conformations (interhelix angle of less than 120° in Figure 7a) twice in the simulation of PLN and in pPLN_rest. In these conformations, Lys3 or Arg14 interacts strongly with the phosphate of a lipid molecule (see Figure 6c), suggesting that these positively charged residues act as membrane anchors. This observation is consistent with the fact that the positively charged amino acid residues are frequently observed in the lipid−solvent boundary of membrane proteins (*52*). Figure 7b shows that pPLN_rest took conformations represented by the L-shaped structure, whereas pPLN took the most open conformations in the three 30 ns MD simulations. Considering that both simulations were conducted for the pPLN, it is clear that conventional MD simulations for several tens of nanoseconds do not provide equilibrium structures of PLN or pPLN in membranes.

DISCUSSION

Consistency of the Simulation and Experimental Data. In this study, we made the following observations about the structure of pPLN. (i) The C-terminal part of the cytoplasmic α-helix is partially unwound by phosphorylation of PLN at Ser16. (ii) The Cα distance between Tyr6 and Met20 in pPLN is ∼2 Å shorter (16.1 ± 0.8 Å) than in PLN (18.1 ± 0.8 Å). (iii) The phosphate at Ser16 in pPLN forms salt bridges with Arg9, Arg13, and/or Arg14, and of these, the salt bridges involving Arg9 and Arg14 act as helix breakers. Although the first observation has previously been made (*21*), the latter two are new and made possible only by utilizing REMD simulations. As already pointed out, it is highly unlikely that conventional MD simulations can sufficiently sampls the conformation of a target protein within several tens of nanoseconds. The structures obtained here readily explain experimental results by NMR and FRET and remove the apparent discrepancy between them.

The increase in the degree of conformational disorder by phosphorylation of PLN at Ser16 agrees with measurements by NMR (*13*). Specifically, the Hα chemical shifts and the backbone NOE data for AFA-pPLN indicated that the loop region around the phosphorylation site becomes longer after phosphorylation. In addition, the backbone order parameters (S^2) of AFA-pPLN indicated that the flexibility of pPLN increases compared with that of PLN. The heteronuclear NOE value of the Ser16 amide backbone in AFA-pPLN was less than 0.6, indicating that a stable salt bridge is unlikely. The free energy landscape of $pPLN_C$ at 310 K (Figure 2b) shows that pPLN likely has several conformational substates containing different salt bridges, consistent with the small NOE value.

Squire et al. reported that the distance between Tyr6 and a fluorophore, *N*-(1-pyrenylmaleimide), attached to Cys24 decreased by 3 Å on phosphorylation. They interpreted the decrease as an elongation of the cytoplasmic α-helix stabilized by formation of a salt bridge between Arg13 and the phosphate at Ser16. Although a direct comparison between FRET measurements and REMD simulations is not possible, REMD simulations showed that the Cα distance between Tyr6 and Met20 (the C-terminal residue in the

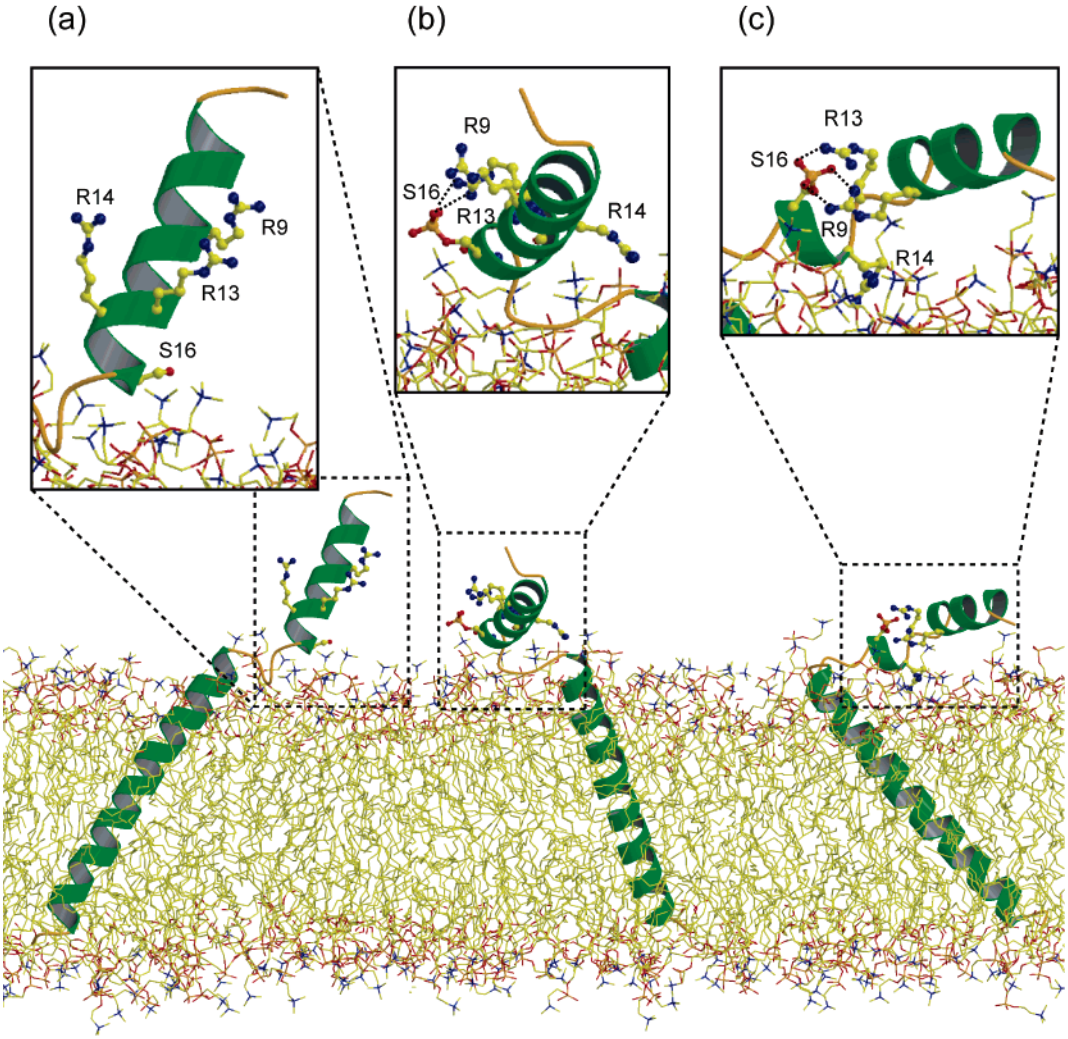

FIGURE 6: Snapshots obtained at 30 ns in MD simulations for (a) PLN, (b) pPLN, and (c) pPLN_rest. The cytoplasmic domains are enlarged in the inset. The side chains of Arg9, Arg13, Arg14, and Ser16 are shown in ball-and-stick form. Salt bridges are represented by dotted lines. This figure was prepared using Molscript (*58*) and Raster3D (*59*).

simulation) decreased by ~2 Å by phosphorylation (Figures 2 and 5), consistent with FRET measurements. However, this was due to a break rather than the elongation of the helix. Thus, our picture on pPLN is consistent with both NMR (*13*) and FRET results (*16*).

Role of the Conformational Changes in the Cytoplasmic Domain of PLN upon Phosphorylation at Ser16. We have studied how the phosphorylation at Ser16 alters the structure of PLN in solution and in membrane, but we do not know yet how the phosphorylation relieves the inhibitory effect of PLN. The current simulation study suggests that the phosphorylation of PLN at Ser16 unwinds the cytoplasmic helix by forming salt bridges between pSer16 and three arginines and thereby reduces the interaction between SERCA and PLN (Figure 8a). Even though pPLN that retains the long cytoplasmic α-helix may still be able to interact with SERCA in a similar way, the population of PLN in such conformations is substantially reduced (clusters Ip-IIIp in Figure 2b). Because the face of the helix available for interaction with SERCA appears to be different between clusters I and II, if we assume PLN in cluster I is able to bind to SERCA, PLN in cluster II will not. Although pPLN in one of the most prominent groups (IIIp, Figure 2b) contains a long helix, the path of the loop connecting to the transmembrane domain is fixed and altered by the salt bridge. Thus, although the change in the distribution of different conformations as revealed by REMD simulations may appear to be rather small at first glance, it is probably not so. It is likely that only pPLN in cluster Ip retains the ability to interact with SERCA in a manner similar to that of unphosphorylated PLN. Then, because cluster Ip is a minor one, relief of inhibitory action of PLN will be explained immediately. We should also consider that there must be a dynamic equilibrium among different conformations. Then, pPLN in clusters Ip and IIp at one moment will take distorted conformations at least for some time. If SERCA can bind Ca^{2+} during that period, the reaction will proceed.

Mutagenesis studies on PLN support this idea. A Ser16Glu mutation in PLN greatly reduces the inhibitory effect of PLN (*53*), suggesting that the salt bridges between Glu16 and Arg9, Arg13, and/or Arg14 induce conformational disorder, resembling those in pPLN. In contrast, single mutations of Arg9, Arg13, and Arg14 to Ala do not substantially reduce the inhibitory effect of PLN (*54*).

The interaction between PLN and PKA is also essential for understanding the relief of the inhibitory effect of phospholamban by phosphorylation, because Ser16 in PLN is phosphorylated by PKA (*3*). Although the X-ray structure

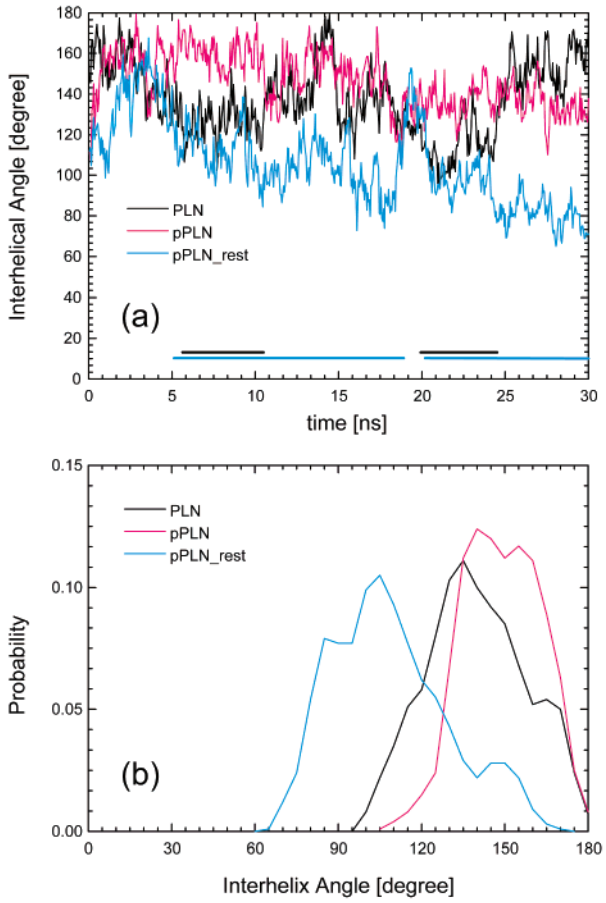

FIGURE 7: Angle between the cytoplasmic (residues 1−16) and transmembrane (residues 22−52) helices observed in the MD simulation of full-length PLN in membranes. (a) Time series and (b) distributions of the angles in PLN (black), pPLN (cyan), and pPLN_rest (magenta). The solid lines represent the durations when PLN or pPLN takes an L-shaped conformation in membranes. Here, an L-shaped conformation is defined as that with an interhelical angle of <120°.

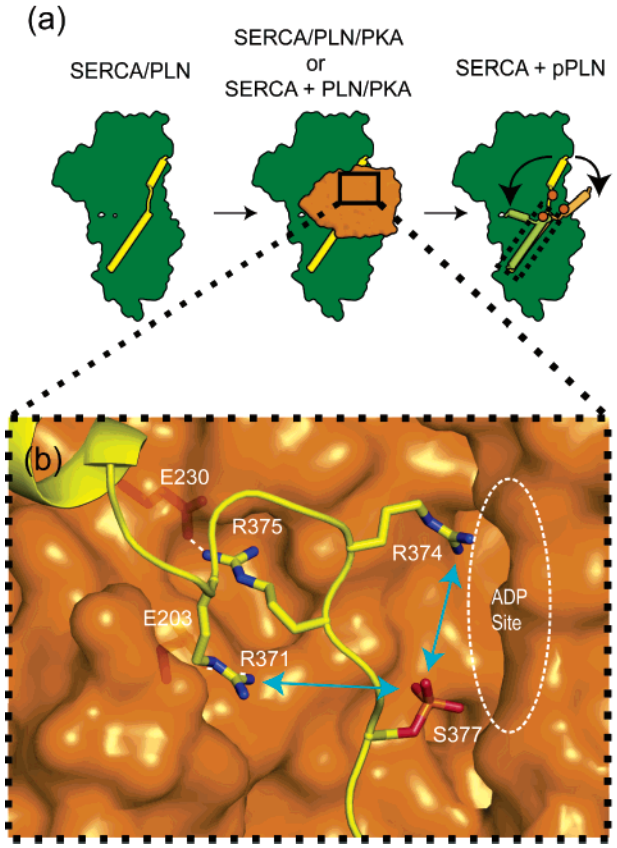

FIGURE 8: Schematic diagram illustrating the functional role of phosphorylation of PLN at Ser16. (a) The binding of PLN to SERCA is inhibited due to the distortion of the helical structure of pPLN. SERCA, PKA, and PLN are colored green, orange, and yellow, respectively. (b) Electrostatic interactions between PKA and an inhibitor peptide observed in the X-ray structure (PDB entry 1JLU). A white dashed line represents the salt bridge between PKA and the inhibitor peptide; cyan arrows represent the interactions that are likely to be required for the release of pPLN from PKA, and the position of ADP in an X-ray structure of the PKA complex with an unphosphorylated inhibitor peptide (PDB entry 1JBP) is shown as a dashed oval. This figure was prepared with Molscript (*58*), Raster3D (*59*), and PyMol (*60*).

of PLN bound to PKA is yet to be determined, an X-ray structure for PKA containing an inhibitory peptide is available, the amino acid sequence of which is similar to that of PLN (*55*, *56*). The inhibitory peptide also has three arginines (Arg371, Arg374, and Arg375) preceding the phosphorylation site (Ser377); they likely play the same functional roles as Arg9, Arg13, and Arg14 of PLN. In the X-ray structure of PKA with the unphosphorylated form of the peptide, Arg371 (equivalent to Arg9 in PLN) and Arg375 (equivalent to Arg14 in PLN) in the inhibitory peptide form salt bridges between Glu230 and Glu203 of PKA, respectively (Figure 8b), whereas Arg374 (equivalent to Arg13 in PLN) in the inhibitory peptide forms a hydrogen bond with ADP. The corresponding arginines in PLN likely form similar salt bridges with PKA before phosphoryl transfer.

pPLN must be released from PKA after phosphorylation by breaking the interaction with PKA and rearranging the salt bridges involving the arginines and pSer16. Recently, an Arg9Cys mutation in PLN was found to cause dilated cardiomyopathy and heart failure (*56*, *57*). Although the mutant does not directly inhibit SERCA2a, it traps PKA and blocks PKA-mediated phosphorylation of wild-type PLN, resulting in a delayed decay of calcium transients in myocytes (*57*). With the available structural and functional information, it appears that the formation of a salt bridge between pSer16 and Arg9 (between Ser377 and Arg371 in the inhibitory peptide) is essential for PLN to be released from PKA after phosphorylation. The Arg9Cys mutant traps PKA presumably because it cannot form the salt bridge (Figure 8b), which works to take different conformations of pPLN in solution. To see if this hypothesis is valid, we need the atomic structure of PLN bound to PKA.

In conclusion, our simulation study has reconciled seemingly opposing results from NMR and FRET studies and proposed a detailed atomic picture on the effects of phosphorylation at Ser16 of phospholamban.

ACKNOWLEDGMENT

We thank T. Tsuda and D. H. MacLennan for many helpful discussions.

SUPPORTING INFORMATION AVAILABLE

Simulation data of full-length PLN or pPLN in membranes, average α-helicity of each residue in PLN, pPLN, and pPLN_rest, and animations of 30 ns MD simulations of

PLN, pPLN, and pPLN_rest with a DOPC lipid bilayer. In the animations, solvent molecules are omitted for clarity. This material is available free of charge via the Internet at http://pubs.acs.org.

REFERENCES

1. MacLennan, D. H., and Kranias, E. G. (2003) Phospholamban: A crucial regulator of cardiac contractility, *Nat. Rev. Mol. Cell Biol. 4*, 566−577.
2. Zamoon, J., Mascioni, A., Thomas, D. D., and Veglia, G. (2003) NMR solution structure and topological orientation of monomeric phospholamban in dodecylphosphocholine micelles, *Biophys. J. 85*, 2589−2598.
3. Tada, M., Kirchberger, M. A., and Katz, A. M. (1976) Regulation of calcium transport in cardiac sarcoplasmic reticulum by cyclic AMP-dependent protein kinase, *Recent Adv. Stud. Card. Struct. Metab. 9*, 225−239.
4. Tada, M., Inui, M., Yamada, M., Kadoma, M., Kuzuya, T., Abe, H., and Kakiuchi, S. (1983) Effects of phospholamban phosphorylation catalyzed by adenosine 3′:5′-monophosphate- and calmodulin-dependent protein kinases on calcium transport ATPase of cardiac sarcoplasmic reticulum, *J. Mol. Cell. Cardiol. 15*, 335−346.
5. Mascioni, A., Karim, C., Zamoon, J., Thomas, D. D., and Veglia, G. (2002) Solid-state NMR and rigid body molecular dynamics to determine domain orientations of monomeric phospholamban, *J. Am. Chem. Soc. 124*, 9392−9393.
6. Kimura, Y., Kurzydlowski, K., Tada, M., and MacLennan, D. H. (1997) Phospholamban inhibitory function is activated by depolymerization, *J. Biol. Chem. 272*, 15061−15064.
7. Asahi, M., Kimura, Y., Kurzydlowski, K., Tada, M., and MacLennan, D. H. (1999) Transmembrane helix M6 in sarco(endo)plasmic reticulum Ca^{2+}-ATPase forms a functional interaction site with phospholamban. Evidence for physical interactions at other sites, *J. Biol. Chem. 274*, 32855−32862.
8. James, P., Inui, M., Tada, M., Chiesi, M., and Carafoli, E. (1989) Nature and site of phospholamban regulation of the Ca^{2+} pump of sarcoplasmic reticulum, *Nature 342*, 90−92.
9. Toyoshima, C., Asahi, M., Sugita, Y., Khanna, R., Tsuda, T., and MacLennan, D. H. (2003) Modeling of the inhibitory interaction of phospholamban with the Ca^{2+} ATPase, *Proc. Natl. Acad. Sci. U.S.A. 100*, 467−472.
10. Toyoshima, C., and Nomura, H. (2002) Structural changes in the calcium pump accompanying the dissociation of calcium, *Nature 418*, 605−611.
11. Metcalfe, E. E., Zamoon, J., Thomas, D. D., and Veglia, G. (2004) $^{1}H/^{15}N$ heteronuclear NMR spectroscopy shows four dynamic domains for phospholamban reconstituted in dodecylphosphocholine micelles, *Biophys. J. 87*, 1205−1214.
12. Zamoon, J., Nitu, F., Karim, C., Thomas, D. D., and Veglia, G. (2005) Mapping the interaction surface of a membrane protein: Unveiling the conformational switch of phospholamban in calcium pump regulation, *Proc. Natl. Acad. Sci. U.S.A. 102*, 4747−4752.
13. Metcalfe, E. E., Traaseth, N. J., and Veglia, G. (2005) Serine 16 phosphorylation induces an order-to-disorder transition in monomeric phospholamban, *Biochemistry 44*, 4386−4396.
14. Kirby, T. L., Karim, C. B., and Thomas, D. D. (2004) Electron paramagnetic resonance reveals a large-scale conformational change in the cytoplasmic domain of phospholamban upon binding to the sarcoplasmic reticulum Ca-ATPase, *Biochemistry 43*, 5842−5852.
15. Karim, C. B., Kirby, T. L., Zhang, Z., Nesmelov, Y., and Thomas, D. D. (2004) Phospholamban structural dynamics in lipid bilayers probed by a spin label rigidly coupled to the peptide backbone, *Proc. Natl. Acad. Sci. U.S.A. 101*, 14437−14442.
16. Li, J., Bigelow, D. J., and Squier, T. C. (2003) Phosphorylation by cAMP-dependent protein kinase modulates the structural coupling between the transmembrane and cytosolic domains of phospholamban, *Biochemistry 42*, 10674−10682.
17. Li, J., Bigelow, D. J., and Squier, T. C. (2004) Conformational changes within the cytosolic portion of phospholamban upon release of Ca-ATPase inhibition, *Biochemistry 43*, 3870−3879.
18. Karim, C. B., Stamm, J. D., Karim, J., Jones, L. R., and Thomas, D. D. (1998) Cysteine reactivity and oligomeric structures of phospholamban and its mutants, *Biochemistry 37*, 12074−12081.
19. Karim, C. B., Marquardt, C. G., Stamm, J. D., Barany, G., and Thomas, D. D. (2000) Synthetic null-cysteine phospholamban analogue and the corresponding transmembrane domain inhibit the Ca-ATPase, *Biochemistry 39*, 10892−10897.
20. Houndonougbo, Y., Kuczera, K., and Jas, G. S. (2005) Structure and dynamics of phospholamban in solution and in membrane bilayer: Computer simulations, *Biochemistry 44*, 1780−1792.
21. Paterlini, M. G., and Thomas, D. D. (2005) The α-helical propensity of the cytoplasmic domain of phospholamban: A molecular dynamics simulation of the effect of phosphorylation and mutation, *Biophys. J. 88*, 3243−3251.
22. Sugita, Y., and Okamoto, Y. (1999) Replica-exchange molecular dynamics method for protein folding, *Chem. Phys. Lett. 314*, 141−151.
23. Berg, B. A., and Neuhaus, T. (1991) Multicanonical Algorithms for 1st Order Phase-Transitions, *Phys. Lett. B 267*, 249−253.
24. Hansmann, U. H. E., and Okamoto, Y. (1993) Prediction of Peptide Conformation by Multicanonical Algorithm: New Approach to the Multiple-Minima Problem, *J. Comput. Chem. 14*, 1333−1338.
25. Hukushima, K., and Nemoto, K. (1996) Exchange Monte Carlo method and application to spin glass simulations, *J. Phys. Soc. Jpn. 65*, 1604−1608.
26. Nakajima, N., Nakamura, H., and Kidera, A. (1997) Multicanonical ensemble generated by molecular dynamics simulation for enhanced conformational sampling of peptides, *J. Phys. Chem. B 101*, 817−824.
27. Sugita, Y., Kitao, A., and Okamoto, Y. (2000) Multidimensional replica-exchange method for free-energy calculations, *J. Chem. Phys. 113*, 6042−6051.
28. Sugita, Y., and Okamoto, Y. (2000) Replica-exchange multicanonical algorithm and multicanonical replica-exchange method for simulating systems with rough energy landscape, *Chem. Phys. Lett. 329*, 261−270.
29. Mitsutake, A., Sugita, Y., and Okamoto, Y. (2001) Generalized-ensemble algorithms for molecular simulations of biopolymers, *Biopolymers 60*, 96−123.
30. Ferrenberg, A. M., and Swendsen, R. H. (1988) New Monte-Carlo Technique for Studying Phase-Transitions, *Phys. Rev. Lett. 61*, 2635−2638.
31. Ferrenberg, A. M., and Swendsen, R. H. (1989) Optimized Monte-Carlo Data-Analysis, *Phys. Rev. Lett. 63*, 1195−1198.
32. Kumar, S., Bouzida, D., Swendsen, R. H., Kollman, P. A., and Rosenberg, J. M. (1992) The Weighted Histogram Analysis Method for Free-Energy Calculations on Biomolecules. 1. The Method, *J. Comput. Chem. 13*, 1011−1021.
33. Morikami, K., Nakai, T., Kidera, A., Saito, M., and Nakamura, H. (1992) PRESTO (PRotein Engineering SimulaTOr): A vectorized molecular mechanics program for biopolymers, *Comput. Chem. 16*, 243−248.
34. Kitao, A., Hayward, S., and Go, N. (1998) Energy landscape of a native protein: Jumping-among-minima model, *Proteins 33*, 496−517.
35. Sugita, Y., and Kitao, A. (1998) Improved protein free energy calculation by more accurate treatment of nonbonded energy: Application to chymotrypsin inhibitor 2, V57A, *Proteins 30*, 388−400.
36. MacKerell, A. D., Bashford, D., Bellott, M., Dunbrack, R. L., Evanseck, J. D., Field, M. J., Fischer, S., Gao, J., Guo, H., Ha, S., Joseph-McCarthy, D., Kuchnir, L., Kuczera, K., Lau, F. T. K., Mattos, C., Michnick, S., Ngo, T., Nguyen, D. T., Prodhom, B., Reiher, W. E., Roux, B., Schlenkrich, M., Smith, J. C., Stote, R., Straub, J., Watanabe, M., Wiorkiewicz-Kuczera, J., Yin, D., and Karplus, M. (1998) All-atom empirical potential for molecular modeling and dynamics studies of proteins, *J. Phys. Chem. B 102*, 3586−3616.
37. Mackerell, A. D., Jr., Feig, M., and Brooks, C. L., III (2004) Extending the treatment of backbone energetics in protein force fields: Limitations of gas-phase quantum mechanics in reproducing protein conformational distributions in molecular dynamics simulations, *J. Comput. Chem. 25*, 1400−1415.
38. Jorgensen, W. L., Chandrasekhar, J., Madura, J. D., Impey, R. W., and Klein, M. L. (1983) Comparison of Simple Potential Functions for Simulating Liquid Water, *J. Chem. Phys. 79*, 926−935.
39. Ding, H.-Q., Karasawa, N., and Goddard, I. W. A. (1992) Atomic level simulations on million particles: The cell multipole method for Coulomb and London nonbond interactions, *J. Chem. Phys. 97*, 4309−4315.
40. Hess, B., Bekker, H., Berendsen, H. J., and Fraaije, J. G. E. M. (1997) LINCS: A linear constraint solver for molecular simulations, *J. Comput. Chem. 18*, 1463−1472.

41. Miyamoto, S., and Kollman, P. A. (1992) SETTLE: An analytical version of the SHAKE and RATTLE algorithms for rigid water molecules, *J. Comput. Chem. 13*, 952−962.
42. Kitao, A., Hirata, F., and Go, N. (1991) The Effects of Solvent on the Conformation and the Collective Motions of Protein: Normal Mode Analysis and Molecular-Dynamics Simulations of Melittin in Water and in Vacuum, *Chem. Phys. 158*, 447−472.
43. Garcia, A. E. (1992) Large-Amplitude Nonlinear Motions in Proteins, *Phys. Rev. Lett. 68*, 2696−2699.
44. Amadei, A., Linssen, A. B. M., and Berendsen, H. J. C. (1993) Essential Dynamics of Proteins, *Proteins 17*, 412−425.
45. Ikeguchi, M. (2004) Partial rigid-body dynamics in NPT, NPAT and NPγ T ensembles for proteins and membranes, *J. Comput. Chem. 25*, 529−541.
46. Feller, S. E., and MacKerell, A. D. (2000) An improved empirical potential energy function for molecular simulations of phospholipids, *J. Phys. Chem. B 104*, 7510−7515.
47. Essmann, U., Perera, L., Berkowitz, M. L., Darden, T., Lee, H., and Pedersen, L. G. (1995) A Smooth Particle Mesh Ewald Method, *J. Chem. Phys. 103*, 8577−8593.
48. Feller, S. E., Zhang, Y. H., and Pastor, R. W. (1995) Computer-Simulation of Liquid/Liquid Interfaces. 2. Surface-Tension Area Dependence of a Bilayer and Monolayer, *J. Chem. Phys. 103*, 10267−10276.
49. Zhang, Y. H., Feller, S. E., Brooks, B. R., and Pastor, R. W. (1995) Computer-Simulation of Liquid/Liquid Interfaces. 1. Theory and Application to Octane/Water, *J. Chem. Phys. 103*, 10252−10266.
50. Sugita, Y., Miyashita, N., Ikeguchi, M., Kidera, A., and Toyoshima, C. (2005) Protonation of the acidic residues in the transmembrane cation-binding sites of the Ca^{2+} pump, *J. Am. Chem. Soc. 127*, 6150−6151.
51. Kabsch, W., and Sander, C. (1983) Dictionary of Protein Secondary Structure: Pattern-Recognition of Hydrogen-Bonded and Geometrical Features, *Biopolymers 22*, 2577−2637.
52. Killian, J. A., and von Heijne, G. (2000) How proteins adapt to a membrane-water interface, *Trends Biochem. Sci. 25*, 429−434.
53. Hoshijima, M., Ikeda, Y., Iwanaga, Y., Minamisawa, S., Date, M. O., Gu, Y., Iwatate, M., Li, M., Wang, L., Wilson, J. M., Wang, Y., Ross, J., Jr., and Chien, K. R. (2002) Chronic suppression of heart-failure progression by a pseudophosphorylated mutant of phospholamban via in vivo cardiac rAAV gene delivery, *Nat. Med. 8*, 864−871.
54. Toyofuku, T., Kurzydlowski, K., Tada, M., and MacLennan, D. H. (1994) Amino acids Glu2 to Ile18 in the cytoplasmic domain of phospholamban are essential for functional association with the Ca^{2+}-ATPase of sarcoplasmic reticulum, *J. Biol. Chem. 269*, 3088−3094.
55. Knighton, D. R., Zheng, J. H., Ten Eyck, L. F., Xuong, N. H., Taylor, S. S., and Sowadski, J. M. (1991) Structure of a peptide inhibitor bound to the catalytic subunit of cyclic adenosine monophosphate-dependent protein kinase, *Science 253*, 414−420.
56. Madhusudan, Trafny, E. A., Xuong, N. H., Adams, J. A., Ten Eyck, L. F., Taylor, S. S., and Sowadski, J. M. (1994) CAMP-dependent protein kinase: Crystallographic insights into substrate recognition and phosphotransfer, *Protein Sci. 3*, 176−187.
57. Schmitt, J. P., Kamisago, M., Asahi, M., Li, G. H., Ahmad, F., Mende, U., Kranias, E. G., MacLennan, D. H., Seidman, J. G., and Seidman, C. E. (2003) Dilated cardiomyopathy and heart failure caused by a mutation in phospholamban, *Science 299*, 1410−1413.
58. Kraulis, P. J. (1991) MOLSCRIPT: A Program to Produce Both Detailed and Schematic Plots of Protein Structures, *J. Appl. Crystallogr. 24*, 946−950.
59. Merritt, E. A. (1994) Raster3D Version 2.0. A program for photorealistic molecular graphics, *Acta Crystallogr. D50*, 869−873.
60. DeLano, W. L. (2002) *The PyMOL Molecular Graphics System*, DeLano Scientific, San Carlos, CA.

BI061071Z